Hydrol. Earth Syst. Sci. Discuss., 12, 7469–7502, 2015
www.hydrol-earth-syst-sci-discuss.net/12/7469/2015/
doi:10.5194/hessd-12-7469-2015

Hydrology and Earth System Sciences Discussions
Open Access

Estimating evapotranspiration with thermal UAV data and two source energy balance models

H. Hoffmann[1], H. Nieto[2], R. Jensen[1], R. Guzinski[1,a], P. J. Zarco-Tejada[2], and T. Friborg[1]

[1]Department of Geosciences and Natural Resource Management, University of Copenhagen, Øster Voldgade 10, 1350 Copenhagen, Denmark
[2]Instituto de Agricultura Sostenible (IAS), Consejo Superior de Investigaciones Científicas (CSIC), Campus Alameda del Obispo, Av. Menéndez Pidal s/n, 14004 Córdoba, Spain
[a]now at: DHI GRAS, Agern Allé 5, 2970 Hørsholm, Denmark

Received: 25 June 2015 – Accepted: 20 July 2015 – Published: 6 August 2015

Correspondence to: H. Hoffmann (helene.hoffmann@ign.ku.dk)

Published by Copernicus Publications on behalf of the European Geosciences Union.

Abstract

Estimating evapotranspiration is important when managing water resources and cultivating crops. Evapotranspiration can be estimated using land surface heat flux models and remotely sensed land surface temperatures (LST) which recently have become obtainable in very high resolution using Unmanned Aerial Vehicles (UAVs). Very high resolution LST can give insight into e.g. distributed crop conditions within cultivated fields. In this study evapotranspiration is estimated using LST retrieved with a UAV and the physically-based, two source energy balance models: the Priestley–Taylor TSEB (TSEB-PT) and the Dual-Temperature-Difference (DTD). A fixed-wing UAV was flown over a barley field in western Denmark during the spring and summer in 2014 and retrieved images of LST is successfully processed into thermal mosaics which serve as model input for both TSEB-PT and DTD. The aim is to assess whether a lightweight thermal camera mounted on a UAV is able to provide data of sufficient quality to obtain high spatial and temporal resolution surface energy heat fluxes. Furthermore, this study evaluates the performance of the two source energy balance (TSEB) model scheme during cloudy and overcast weather conditions. This is feasible due to the low data retrieval altitude compared to satellite thermal data that are only available during clear skies and sunny conditions. Flux estimates from TSEB-PT and DTD are compared and validated against field data collected using an eddy covariance system located at same site at which the UAV flights were conducted. Furthermore, spatially distributed evapotranspiration patterns are evaluated using known irrigation patterns. Evapotranspiration is well estimated by both TSEB-PT and DTD with DTD as the best predictor. The DTD model provides results comparable to studies estimating evapotranspiration with satellite retrieved LST and physical land-surface models. This study shows that the UAV platform and the lightweight thermal camera provide high spatial and temporal resolution data valid for model input and for other potential applications requiring high resolution and consistent LST. Lastly, this study explicates thermal UAV data processing and the mosaicking of images into ortho-photos suited for model input.

HESSD
12, 7469–7502, 2015

Estimating evapotranspiration with thermal UAV data

H. Hoffmann et al.

1 Introduction

Evapotranspiration (latent heat flux) serves as a key component in both hydrological and land-surface energy processes. However, it is often estimated indirectly because spatially distributed, physical measurements of evaporated water are cumbersome. Provided information on net solar radiation (R_n) and sensible heat flux (H), the latent heat flux (LE) can be estimated as a residual using the assumption of surface energy balance in cases with no significant heat advection:

$$R_n = H + \mathrm{LE} + G \tag{1}$$

where G is soil heat flux, which is often estimated as a fraction of R_n if direct measurements are not available. All terms in the above surface energy balance equation are related to the land surface temperature (LST). Since the 1980s estimates of evapotranspiration have been obtained through remotely sensed LST and advanced land surface heat flux models accounting for vegetation, soil and atmospheric conditions (Anderson et al., 1997; Kalma et al., 2008) and a large number of heat flux models exist with significant variations in physical system conceptualization and input requirements (Boulet et al., 2012; Kustas and Norman, 1996; Stisen et al., 2008). Norman et al. (1995) applied the two source energy balance model (TSEB) (Shuttleworth and Wallace, 1985) to remotely sensed data and this modelling scheme has proven to estimate reliable surface heat fluxes over cropland, rangeland and forest as well as at various spatial scales (Anderson et al., 2004; Norman et al., 2003). The TSEB modelling scheme generates robust estimates of surface heat fluxes despite a simple solution scheme demanding relatively few input data. It is thermally based and developed to be operational using satellite images (Anderson et al., 2011). The significant contribution provided by the original TSEB model, is the partition of remotely sensed LST observations into two layers; a soil temperature and a canopy temperature, which enables a partition of heat flux estimations into soil and canopy respectively. The temperature partition allows the model to avoid the need for estimating the so called excess resistance term, which is difficult to derive reliably. As most of the remote sensing systems only provide a single radiometric observation, Norman et al. (1995) proposed applying an iterative process to derive the canopy and soil temperature. It is based on an initial guess of canopy transpiration, which was based on the Priestley and Taylor potential evapotranspiration (Priestley and Taylor, 1972). This approach is hereafter called TSEB-PT in order to differentiate it from other TSEB approaches such as TSEB-LUE (Houborg et al., 2012), based on the Light Use Efficiency concept, or TSEB-2ART, which utilizes dual angle LST observations for direct retrieval of soil and canopy temperatures (Guzinski et al., 2015). Remotely sensed surface temperature observations may deviate from the actual surface temperature by several degrees Kelvin due to atmospheric and surface emissivity effects. Consequently thermally-based models utilizing satellite inputs that do not address this issue are prone to produce less accurate results. Trying to overcome this issue, Norman et al. (2000) developed the Dual-Temperature-Difference model (DTD), incorporating two temperature observations into the TSEB modelling scheme; one conducted an hour after sunrise and another conducted later the same day when flux estimations are desired. One hour after sunrise, the surface heat fluxes are minimal and observations acquired at this time represent a "starting point" for the temperatures collected later the same day. By adding a second set of observations to each model run, DTD attempts to minimize the bias errors due to inaccurate remote sensing retrievals of temperature. Obtaining a set of LSTs at one hour past sunrise is, however, rarely possible when relying on polar orbiting satellites, due to their limited overpass times. Guzinski et al. (2013) succeeded in producing surface energy flux estimates using the DTD model and replacing the early morning observation with night observations conducted with the MODIS sensor aboard the Aqua polar orbiting satellite. Nevertheless, there is a shortcoming in the temporal resolution of the satellite observations, especially in areas prone to overcast weather conditions as satellite thermal infrared observations cannot penetrate clouds. The inability to provide data in overcast situations applies to all satellite sensors except those operating in the microwaves region. The spatial resolution of thermal infrared satellite data is on average

HESSD
12, 7469–7502, 2015

in the order of tens to thousands meters and is also regarded as being too low for some applications. For example, Guzinski et al. (2014) downscaled fluxes estimated from MODIS data with the use of Landsat data (from 1 km to 30 m) to ensure an accurate model validation against eddy covariance systems. This, however, resulted in serious degradation in the temporal resolution of the downscaled estimates.

Unmanned aerial vehicles (UAVs) (or Remotely Piloted Aircraft System, RPAS, in its most recent terminology) enable a critical improvement for both spatial and temporal resolution of remotely sensed data. UAVs can operate at any specific time of day and year provided that strong wind and rain are absent. Therefore, the UAV platform permits data acquisition one hour after sunrise, granting inputs in better accordance with the original DTD requirements and during overcast conditions (Hunt Jr. et al., 2005). When UAV data are combined with the presented heat flux models, very detailed output maps are generated providing insight into heat flux variations at centimeter scale. This spatial scale enables a better analysis between different stages of plant growth providing valuable information for e.g. farmers when managing their crops. There is rapidly growing interest in the potential of UAV data particularly in the science of precision agriculture but also in a range of different scientific and commercial communities (Díaz-Varela et al., 2015; Gonzalez-Dugo et al., 2014; Swain et al., 2010; Zarco-Tejada et al., 2013, 2014). As scientists strive to understand the potential of UAVs and the new applications to which they are suited, the development of efficient workflows, operational systems and improved software that capture and process UAV data are continuing (Harwin and Lucieer, 2012; Lucieer et al., 2014; Turner et al., 2012; Wallace et al., 2012). However, research in UAV possibilities and limitations is still at an early stage and UAV operations in flux as well as hydrological sciences are still an unaccustomed territory.

In this study energy balance components are estimated using LST retrieved with a UAV as input for the physically-based, two source energy balance models: TSEB-PT and DTD. The aim is to assess whether a lightweight thermal camera installed on board a UAV is able to provide data of sufficient quality to attain high spatial and temporal resolution surface energy heat fluxes. Besides facilitating high resolution LST,

HESSD
12, 7469–7502, 2015

the UAV platform enable the application of TSEB-PT and DTD models in cloudy and overcast weather conditions. Model outputs are spatially validated with known irrigation patterns and quantitatively validated with data from an eddy covariance system located at the same barley field over which the UAV flights were conducted. Additionally, this study outlines the steps for processing the thermal UAV data and mosaicking images into ortho-photos suited for model input.

2 Site

The TSEB models are applied in a HOBE (Hydrological OBsErvatory) site within the Skjern River catchment in western Denmark (UTC +1 time zone) (see Fig. 1). The site is located in the maritime climate zone where mild winters and cold summers result in a mean annual temperature of 8.2 °C and a mean annual precipitation of 990 mm. Westerly wind is prevailing and windy conditions are common. Cloudy and overcast weather conditions are frequent. The land is cultivated and consists predominantly of sandy soils with seasonally varying crop types (Ringgaard et al., 2011). During the UAV campaign (spring and summer 2014) fields were cultivated with barley. The overall area is somewhat heterogeneous consisting of three barley fields separated by a gravel road to the south and a row of conifers to the west. Conifers are bordering the barley fields at several places. An eddy covariance system is mounted in the middle of the site (black square in Fig. 1).

3 Method

3.1 TSEB-PT

The original TSEB model developed by Norman et al. (1995) is a two-layer model of turbulent heat exchange. The "two-layer" implies that observations of remotely sensed directional radiometric surface temperature are split into two layers: canopy (T_C) and soil (T_S) temperatures. This allows the computation of sensible and latent heat flux from canopy and soil separately and enables a simpler parameterization of resistances compared to single layer models (Monteith, 1965) as no empirical excess resistance adjustment is needed for the calculation of the bulk sensible heat flux (Norman et al., 1995).

In the TSEB modelling scheme the directional radiometric surface temperature $T(\theta)_R$ is assumed to be an ensemble of vegetation and soil temperatures based on the following equation:

$$T(\theta)_R \approx \left(f_\theta T_C^4 + (1 - f_\theta) T_S^4\right)^{0.25} \tag{2}$$

where f_θ is the fraction of view of the radiometer occupied by vegetation (determined through the view zenith angle θ). The first estimation of canopy sensible heat flux is derived using the Priestley–Taylor approximation (Priestley and Taylor, 1972) and subsequently, a canopy temperature can be derived and a partition of LST into soil and canopy temperatures is possible using Eq. (2). The Priestley–Taylor approximation assumes unstressed vegetation transpiring at potential rate and an initial alpha value of 1.26 is chosen according to De Bruin and Keijgman (1979). At the initial state, a neutral atmospheric stability is assumed, hence Obukhov length approaches infinity. With those assumptions, TSEB can compute the combined soil and canopy sensible and latent heat fluxes. Once these are estimated, Obukhov length can be re-calculated according to Brutsaert (2005) and the model re-run. If the first estimate of Priestley–Taylor transpiration is wrong, latent heat flux from soil will be less than zero (representing the unlikely event of condensation during midday), and the model will be rerun iteratively using a lower alpha in the Priestley–Taylor approximation. Calculations will then be repeated until latent heat flux of soil equals zero and realistic values are obtained. The most important equations for the TSEB model when used in the present context are described below.

Net solar radiation (R_n) represents the available energy in the surface energy balance and is computed as the sum of short- and longwave incoming and outgoing radiation $R_{s,\,in}$,$R_{s,\,out}$,$R_{l,\,in}$,$R_{l,\,out}$ respectively:

HESSD
12, 7469–7502, 2015

$$R_n = (R_{s,\,in} - R_{s,\,out}) + (R_{l,\,in} - R_{l,\,out}) \tag{3}$$

$$R_{s,\,in} - R_{s,\,out} = R_{s,\,in}(1-\alpha) \tag{4}$$

$$R_{l,\,in} - R_{l,\,out} = \epsilon_{surf}\epsilon_{atm}\sigma T_A^4 - \epsilon_{surf}\sigma T(\theta)_R^4) \tag{5}$$

where α is the combined vegetation and soil albedo, σ is Stefan–Boltzman constant, T_A is air temperature (K), $T(\theta)_R$ is radiometric land surface temperature (K), ϵ_{surf} is combined vegetation and soil emissivity and ϵ_{atm} is atmosphere emissivity computed as in (Brutsaert, 1975):

$$\epsilon_{atm} = 1.24(\frac{e_a}{T_A})^{0.14286} \tag{6}$$

where e_a is vapor pressure (mb).

Sensible (H) and latent heat fluxes (LE) are computed in several steps and the key equations are described in the following. H is a sum of its canopy and soil components H_C and H_S:

$$H = H_C + H_S = \rho c_p \frac{T_{AC} - T_A}{R_A} \tag{7}$$

$$H_C = \rho c_p \frac{T_C - T_{AC}}{R_X} \tag{8}$$

$$H_S = \rho c_p \frac{T_S - T_{AC}}{R_S} \tag{9}$$

where ρ is air density ($kg\,m^{-3}$), c_p is specific heat of air ($J\,kg^{-1}\,K^{-1}$), R_A is the aerodynamic resistance to heat transport in the surface layer ($s\,m^{-1}$), R_X is boundary layer resistance of the leaf canopy ($s\,m^{-1}$), R_S is resistance to heat transport from the soil surface ($s\,m^{-1}$) and T_{AC} is inter-canopy air temperature computed with T_A, T_S, T_C, and resistances. For detailed resistance definitions see Norman et al. (1995).

Discussion Paper | Discussion Paper | Discussion Paper | Discussion Paper |

HESSD

12, 7469–7502, 2015

Estimating evapotranspiration with thermal UAV data

H. Hoffmann et al.

Latent heat flux for canopy and soil components (LE_C) and (LE_S), are estimated as a residual using surface energy balance:

$$LE_C = \Delta R_n - H_C \tag{10}$$

$$LE_S = R_{n,S} - G - H_S \tag{11}$$

where ΔR_n is energy divergence for the canopy, $R_{n,S}$ is the net radiation reaching the soil and G is soil heat flux computed following (Liebethal and Foken, 2007):

$$G = 0.3R_{n,\,S} - 35 \tag{12}$$

with all energy fluxes expressed in $W\,m^{-2}$.

In this study the "series" resistance network approach (in contrast to "parallel") is used for both TSEB-PT and DTD, allowing heat fluxes from vegetation and soil to interact and hence improving results during dry conditions when evapotranspiration is relatively small (Kustas and Norman, 1999; Norman et al., 2000; Guzinski et al., 2014)

3.2 DTD

The DTD model described in Norman et al. (2000) is a further development of the TSEB modelling scheme. DTD similarly divides the observed LST into vegetation and soil temperatures and computes surface energy balance components following virtually the same procedure. However, DTD accounts for the discrepancy between the fact that the TSEB modelling scheme is sensitive to the temperature difference between land surface and air, and that absolute temperature retrievals from remote sensing data might be regarded as inaccurate. This is accounted for by adding an additional input dataset: LST retrieved one hour after sunrise when energy fluxes are minimal. The modelled fluxes are hence based on a temperature difference between the two observation times, which is a more robust parameter compared to a single retrieval of remotely sensed temperature as it minimizes consistent bias in the temperature estimates. The essential equation that differs between TSEB-PT and DTD is the one computing sensible heat flux. In the series implementation of DTD the linear approximation

HESSD
12, 7469–7502, 2015

of Eq. (2) is taken together with Eqs. (7) to (9) and applied at midday and one hour after sunrise and subsequently subtracted from each other to arrive at the following:

$$H_i = \rho c_p \left[\frac{(T_{R,i}(\theta_i) - T_{R,0}(\theta_0)) - (T_{A,i} - T_{A,0})}{(1 - f(\theta_i))R_{S,i} + R_{A,i}} \right] + H_{C,i} \left[\frac{(1 - f(\theta_i))R_{S,i} - f(\theta_i)R_{X,i}}{(1 - f(\theta_i))R_{S,i} + R_{A,i}} \right] \quad (13)$$

where subscripts i and 0 refer to observations at midday and one hour after sunrise respectively. Since the early morning (time 0) sensible heat fluxes are negligible they are omitted in the above equation.

Computations of soil heat flux (G) also differ because the difference in radiometric temperature between midday and sunrise observations can be used as an approximation of the diurnal variation in soil surface temperature. Soil heat flux computations are derived from the soil heat flux model of Santanello and Friedl (2003). Finally, this study uses a modification to the R_S equation in the DTD model to better account for the temperature difference between the canopy and soil in varying canopy conditions (Guzinski et al., 2015). For an in-depth review of the TSEB-PT and DTD equations, see Guzinski et al. (2014, 2015).

4 Data description and processing

4.1 UAV campaign

UAV data was collected on seven days distributed evenly during spring and summer 2014 (Table 1). In total 19 flights were conducted, of which 7 were flown early in the morning, constituting the additional input data for the DTD model. The entire airborne campaign thus resulted in 12 sets of input data for the TSEB-PT and DTD model. Dates with (c) in Table 1 mark days where the UAV flights were conducted in cloudy or overcast conditions.

The fixed-wing UAV platform used for airborne operations has a wing span of 2.2 m and is capable of carrying a payload of 2 kg for approximately 25 min in the air. With a speed of 60 $\mathrm{km\,h^{-1}}$ and flying height of 90 m above ground, the 400 m × 400 m site area was covered in a single flight. The UAV was controlled by the SkyCircuits Ltd SC2 autopilot in a dual redundant system with separate laptop and transmitter control. Communication between autopilot and ground is performed by a radio link which transmits position and attitude. Landing is conducted manually using the transmitter. SkyCircuits Ground Control Station software is used for generating the flight route and for visual inspection while UAV is in the air.

Thermal data and image processing

Thermal data was collected with an Optris PI LightWeight Kit consisting of a miniaturized PC and an Optris PI 450 LW infrared camera. PC and camera together weight 380 g which enable their mounting within the UAV. Thermal images are stored at 16 bit radiometric resolution. According to manufacturer specifications, the system has an accuracy of ±2 °C or ±2 % at an ambient temperature of 23 ± 5 °C. The thermal sensor detects infrared energy in the 7.5–13 µm thermal spectrum and surface temperatures were computed automatically using a fixed emissivity of 1. The thermal detector collects an image array of 382 × 288 pixels with a nadir viewing footprint of 50 m × 40 m $\mathrm{image^{-1}}$ at 90 m flying height, resulting in an effective ground resolution of approx. 0.13 $\mathrm{m\,pixel^{-1}}$.

Time synchronization between camera and autopilot is necessary in order to link the logged GPS and rotation position with each image. This was performed before launching the UAV with a USB GPS connected to the lightweight PC and synchronizing the PC time with the GPS clock. Timestamps were recorded in UTC time and accurate to within 1 s, which resulted in a position accuracy of approximately 17 m when flying 60 $\mathrm{km\,h^{-1}}$. Re-calculation of camera position is thus necessary and was performed using a self-calibrating bundle adjustment in Agisoft PhotoScan software (Professional Edition version 1.0.4).

Discussion Paper | Discussion Paper | Discussion Paper | Discussion Paper |

HESSD

12, 7469–7502, 2015

Estimating evapotranspiration with thermal UAV data

H. Hoffmann et al.

Between 600 and 900 images were collected for each flight with camera recording in continuous mode, triggering an image every second. Generally half of the images were suitable for further processing. Non-suitable images may occur due to strong gusts of wind affecting flight velocity which can lead to poor quality recording and blurry images. Images collected during take-off and landing were likewise discarded. In addition to re-calculating camera positions, the self-calibrating bundle adjustment computed three dimensional point clouds from which thermal ortho-mosaics were built using a mean value composition. Thermal ortho-mosaics were used as driving input to TSEB-PT and DTD. No ground control points were used nor needed during camera alignment and bundle adjustment. Resulting resolution on thermal mosaics from midday flights was 0.20 m. Figure 2 shows a small part of thermal mosaic from 18 June 2014 12:00 UTC and provide a sense of the high resolution data. However, the software was not able to mosaic the early morning data, presumably because temperatures were too homogeneous to enable the detection of common features between images needed for the bundle adjustment. Consequently, LST from early morning flights were extracted manually and only the average LST for the barley fields was used as the additional data input for DTD model runs. Using an average is a satisfying representation of sunrise LST because of its homogenous nature.

The view zenith angle (Sect. 3.1) of ortho-mosaics was set to 0° for all pixels, hence the largest possible amount of soil was assumed visible. The maximum view zenith angle of the thermal camera is 15° and setting a theoretical view zenith angle to 0° could lead to a small overestimation of latent heat flux. Using a maximum value composition when generating thermal ortho-mosaics may have accommodated any bias due to 0° view zenith angle in models. However, a mean value composition was used because the mosaics produced with this method compared well with mosaics produced manually in which the edges of the images were eliminated due to vignetting effects. Using a mean value composition is thus assumed to enable the usage of entire images without eliminating or correcting vignetting edges and hence allowing a larger coverage and image overlap.

HESSD
12, 7469–7502, 2015

Title Page
Abstract | Introduction
Conclusions | References
Tables | Figures
◀| |▶
◀ ▶
Back | Close
Full Screen / Esc
Printer-friendly Version
Interactive Discussion

4.2 Extraction of flux values from model output maps

In order to compare modelled R_n, H and LE to measurements from the eddy covariance system, a single representative values from each TSEB-PT and DTD output map have to be extracted in accordance with the eddy flux tower footprint. Each eddy flux measurement represents an area for which the size, shape and location are determined by surface roughness, atmospheric thermal stability and wind direction at a given time – in this case UAV flight times. Sensible and latent heat fluxes are extracted from TSEB-PT and DTD maps using a two-dimensional footprint analysis approach as described in Detto et al. (2006). The twelve footprint outputs were applied to corresponding maps of sensible and latent heat fluxes by weighing each modelled pixel according to the contribution of that pixel's location to the measured flux. Net radiation measurements have footprints that are much smaller than sensible and latent heat flux measurements and values from R_n output maps were extracted from a 5 m × 5 m area on the barley field close to the eddy flux tower.

4.3 Auxiliary data

4.3.1 Model data

An eddy covariance system consisting of a Gill R3-50 sonic anemometer and a LI-7500 open path infrared gas analyzer is mounted 6 m above ground in the middle of the site (see Fig. 1). Wind components in three dimensions and concentrations of water vapor were measured at 10 Hz. Meteorological data used in the two models was collected at the same tower. Meteorological input data comprised air temperature, wind speed, atmospheric pressure, vapor pressure deficit and short- and longwave incoming radiation.

Further model inputs were leaf area index (LAI), canopy height, effective leaf size, fraction of vegetative canopy that is green, vegetation fractional cover, emissivity and albedo from both vegetation and soil. LAI measurements were obtained with a canopy analyzer LAI2000 instrument three times during UAV campaign: 21 May, 3 and 18 June 2014. Averages of LAI from six locations collected from the northern and southern barley fields were computed. LAI values used for each flight day were extracted from linear interpolation, taking measured canopy height into account as a covariate. Two linear fits were produced; one representing the flourishing period, up to and including 22 May 2014 and another representing the period of senescence, from 18 June 2014 onwards. Canopy height, leaf size and fraction of vegetative canopy that is green were estimated in situ for each flying day, as a mean extracted from same locations at which LAI measurements were obtained. Vegetation fractional cover and emissivity for vegetation and bare soil were obtained from Guzinski et al. (2014). Albedo was estimated from the incoming and outgoing short wave radiation measured at the eddy flux tower. Albedo for bare soil was retrieved before barley started showing on surface and was kept fixed (although some changes are expected with soil humidity) whereas albedo for vegetation was retrieved for each flying day and hence varied throughout the season.

4.3.2 Validation data

Sensible and latent heat fluxes for validation of model outputs were computed from the eddy covariance system using EddyPro 5.1.1 software. Computations include two dimensional coordinate rotation, block averaging of measurements in 30 min windows, corrections for density fluctuations (Webb et al., 1980), spectral corrections (Moncrieff et al., 2005, 1997) and measurement quality checking according to Mauder and Foken (2006). Furthermore, the computed heat fluxes were subject to an outlier quality control following procedures described in Papale et al. (2006). Short- and long-wave, incoming and outgoing radiation and soil heat fluxes were measured with a four component Hukseflux thermal sensor (model NR01) and heat flux plate (model HFP01) respectively. Gaps in the validation dataset, which can occur due to either instrumentation errors causing lack of measurements or measurements being discarded during quality controls, were filled according to Reichstein et al. (2005). Any residual in the validation dataset when applying the surface energy balance expression, was assigned to latent

HESSD
12, 7469–7502, 2015

heat flux as recommended by Foken et al. (2011). This assures energy balance closure and comparability with TSEB-PT and DTD modelled fluxes.

5 Results and discussion

TSEB-PT and DTD models are executed twelve times with data collected on seven days during the spring and summer of 2014. Spatially distributed maps of net radiation and sensible and latent heat fluxes are attained.

5.1 Evapotranspiration maps and spatial validation

Twelve evapotranspiration maps computed with DTD are shown in Fig. A1. Patterns of evapotranspiration within the barley fields are alike for TSEB-PT and DTD maps. The maps differ in size due to different flight routes, which are determined by wind direction and velocity at the given day. Forest areas adjacent to the barley fields are excluded from the final evapotranspiration maps because LAI (which impacts the radiation divergence in the canopy, surface roughness and indirectly the net radiation through parameters such as albedo), vegetation height (which influences surface roughness and hence the resistances to heat transfer) and fraction of vegetation that is green (which influences the initial canopy transpiration) are only representative for cultivated areas. As expected, evapotranspiration maps reveal large variations determined primarily by time of year and time of day – dates and hours with potentially large incoming solar radiation (summer and midday) contain potential for largest evapotranspiration. The evapotranspiration maps are detailed and accurate enough to show differences between crops and tramlines, and maps from 18 June 2014 and onwards reveal significant differences within the barley fields: patterns of approx. 20 m wide darker areas running parallel to the tramlines illustrate less evapotranspiration. These locations correspond to areas where irrigators running in tramline trails have not been able to irrigate as intensively as areas closer to the tramlines. These areas likely contain less healthy plants, produc-

HESSD
12, 7469–7502, 2015

ing higher LST and lower evapotranspiration rates. The evapotranspiration patterns are commencing but less pronounced in maps from 22 May 2014. Recognition of very likely patterns of evapotranspiration within fields bodes well for quality of collected thermal data and processing of images.

5.2 Comparison between measured and modelled fluxes

Modelled fluxes attained by applying footprints to model outputs (Sect. 4.2) and measured fluxes from the eddy covariance system are shown in Table 2. Figure 3a–c show modelled vs. measured fluxes and a statistical comparison is presented in Table 3. Accurate computation of net radiation (R_n) is essential in order to satisfactory model sensible and latent heat fluxes. Modelled R_n consists of short- and longwave incoming and outgoing radiation ($R_{s,\,in}$, $R_{s,\,out}$, $R_{l,\,in}$, $R_{l,\,out}$) of which $R_{s,\,in}$ is provided as model input from eddy tower measurements. This contributes positively to the agreement between modelled and measured R_n but it cannot be assigned to model performance or the quality of collected temperature data. However, it can be seen from Eq. (5) that LST collected with UAV ($T(\theta)_R$), is also part of R_n calculations, and hence a bad retrieval of this parameter would have a negative effect on estimated R_n. Calculations for R_n are alike in TSEB-PT and DTD and generally in good agreement with measured R_n with a RMSE value of 44 $W\,m^{-2}$ and a R value of 0.98 (Table 3). Simulated R_n from 10 April and 2 July 2014 are in less good agreement with measured R_n and are underestimated with 88 and 96 $W\,m^{-2}$ respectively (Table 2). The underestimation on 10 April 2014 might be due to that at this time, the majority of surface comprises of soil, which albedo and emissivity varies with water content. If the soil was comparably wetter compared to the time of albedo and emissivity estimations for model input, LST would be underestimated. An underestimation of LST correlates well with the underestimation of H seen on same date (10 April 2014) with TSEB-PT and DTD estimates of 15 and 20 $W\,m^{-2}$ respectively, compared to measured H of 87 $W\,m^{-2}$ (Table 2). The underestimation of R_n on 2 July 2014 could be due to scattered clouds during LST retrievals. This is only

HESSD
12, 7469–7502, 2015

speculative since it was only noted that data collected this day was either during cloudy or overcast situations. However, it is worth mentioning that data collected during conditions with scattered clouds and hence quickly changing irradiance, would lead to large variations in retrieved LST during a single flight. LST collected with UAVs are instantaneous but also a mosaic of instantaneous LST collected in a time span of 20 min. Comparing this kind of measurement to a 30 min flux average from eddy covariance system can lead to substantial disagreement (Kustas et al., 2002). Sensible heat fluxes are generally well estimated by both models. TSEB-PT sensible heat fluxes are consistently underestimated, however with a better correlation coefficient (r) (in contrast to RMSE and MAE) than DTD which reveals a steadier trend prediction in TSEB-PT (see Fig. 3b). The DTD model computes slightly more scattered sensible heat fluxes but results do not show any systematic errors – they are centered around measured values and are generally in better accordance with measured fluxes with RMSE and MAE values of 59 and 49 $\mathrm{W\,m^{-2}}$ respectively, compared to TSEB-PT RMSE and MAE values of 85 and 75 $\mathrm{W\,m^{-2}}$. Soil heat fluxes (G) are generally simulated poorly by both TSEB and DTD. However the magnitude of G is small compared to the remaining surface energy fluxes and therefore has a comparably small impact on LE estimations even though it is computed as a residual of R_n, H and G. Modelled latent heat flux is in good agreement with measured latent heat fluxes. As a consequence of underestimation of sensible heat flux in TSEB-PT simulations, overestimation of TSEB-PT latent heat flux is seen (Fig. 3c). DTD latent heat flux is again more scattered but with lower RMSE and MAE values of 67 and 57 $\mathrm{W\,m^{-2}}$ respectively, compared to TSEB-PT RMSE and MAE values of 94 and 84 $\mathrm{W\,m^{-2}}$. The DTD algorithm generally produces results in better accordance with measurements and is concluded to be a better predictor of heat fluxes than TSEB-PT in the presented setup. This suggests a consistent bias in the UAV derived LST which can be corrected by subtracting the early morning observations from the midday ones and demonstrate the robustness and added utility of the DTD approach. A calibration of the camera with in situ temperatures would likely have improved TSEB LE and H computations together with conversion of brightness temperature to actual LST using a known surface emissivity and longwave atmospheric data.

Comparing statistical parameters in this study to the study made by Guzinski et al. (2014) on the same field site with the same models but driven by satellite data, similar results are seen when only Landsat images are used. Guzinski et al. (2014) obtained RMSE values of 46 $\mathrm{W\,m^{-2}}$ for R_n, 56 $\mathrm{W\,m^{-2}}$ for H and 66 $\mathrm{W\,m^{-2}}$ for LE, obtained using TSEB-PT and Landsat data (Table 2, column $\mathrm{ND_H}$ in Guzinski et al., 2014) which are comparable to RMSE values of 44 $\mathrm{W\,m^{-2}}$ for R_n, 59 $\mathrm{W\,m^{-2}}$ for H and 67 $\mathrm{W\,m^{-2}}$ for LE, obtained using DTD in this study. r is likewise similar between the two studies. However, when both MODIS and Landsat data were used to disaggregate DTD flux estimates, modelled sensible and latent heat fluxes were in better agreement with the observed fluxes (Table 2, column EF in Guzinski et al., 2014). Also, when comparing results in this study with those computed with the original DTD model (Norman et al., 2000) and several other studies seeking to estimate surface energy balance components from remotely sensed data (Colaizzi et al., 2012; Guzinski et al., 2013; Norman et al., 2000), the results in the present study are in the same order of agreement.

The majority of data is retrieved under cloudy or overcast conditions. Data collected during sunny conditions are enclosed by black circles in Fig. 3a–c. Fluxes from sunny, cloudy and overcast days cannot immediately be categorized as being different from one another when looking at Fig. 3a–c. Table 4 shows statistical parameters calculated using only data from days with cloudy or overcast weather conditions. RMSE and MAE are better for both R_n, H and LE for both models, except for the MAE and MAE as percentage of measured fluxes for H computed with TSEB-PT which increased to 50 from 49 $\mathrm{W\,m^{-2}}$ and to 78 from 52 % respectively. r values for R_n are almost alike for data only including cloudy and overcast conditions and data also including sunny condition with values of 0.99 and 0.98 respectively. r is worse for H but better for LE for both models when looking at data that only includes cloudy and overcast conditions (see Tables 3 and 4). Statistical parameters presented in Table 4 and the overall good results in the present study compared to above mentioned studies using satellite data (hence data collected in sunny conditions), validate the application of TSEB-PT and DTD models in cloudy and overcast weather conditions.

6 Conclusions and outlook

Land surface temperatures (LST) were obtained with a lightweight thermal camera mounted on a UAV with the ability to cover a 400 m × 400 m barley field in both sunny, cloudy and overcast weather conditions. Thermal images were successfully generated into mosaics that served as driving input for the two source energy balance models: TSEB-PT and DTD. Simulated net radiation, sensible and latent heat fluxes were in good agreement with flux observations from an eddy covariance system located at same barley field at which the UAV flights were conducted, with the DTD model as the better predictor. This was expected since the DTD model accounts for the bias in remotely sensed LST (likely to be present in the lightweight thermal camera retrievals) with an additional set of observations retrieved one hour after sunrise. Irrigation system patterns on the barley field agree with the spatially distributed evapotranspiration patterns produced by both models. Comparing simulated results to other studies estimating surface energy fluxes from heat flux models and remotely sensed LST reveal that the UAV platform and the lightweight thermal camera provide good quality, high spatial and temporal resolution data. Such data can be used for model input and for other potential applications requiring high resolution and precise LSTs. Additionally, the UAV platform accommodated validation of the applicability of the TSEB modelling scheme in cloudy and overcast weather conditions which was possible due to the low altitude retrieval of LST compared to satellite retrievals of LST which are only feasible during clear sky conditions. The dataset retrieved during only cloudy and overcast conditions generally generated similar but slightly better statistical parameters than the dataset that also included sunny conditions.

Future improvements will incorporate spatially distributed optical data into the two source energy balance models in order to estimate spatially varying ancillary variables

HESSD
12, 7469–7502, 2015

such as albedo, leaf area index or canopy height. This would enable flux estimations in areas with heterogeneous vegetation types and should have a positive effect on estimations over maturing crops when differences in irrigation may have impacted their developmental stage. Extending present setup to other land cover types would further strengthen the applicability of thermal UAV data and model scheme. A calibration of thermal camera with in situ temperatures should improve TSEB-PT results with a potential positive effect on DTD results as well.

Acknowledgements. This work was funded by the VILLUM FOUNDATION through the HOBE project. Thanks to Lars Rasmussen and Anton Thomsen for their work in the field that among others ensure flux tower measurements. Also thanks to the Quantalab team at IAS, especially Alberto Hornero Luque, for helping out with thermal camera settings and to Gorka Mendiguren González for explaining footprint applications. Lastly, thanks to Arko Lucieer and his team at University of Tasmania for providing general UAV supervision.

References

Anderson, M. C., Norman, J. M., Diak, G. R., Kustas, W. P., and Mecikalski, J. R.: A two-source time-integrated model for estimating surface fluxes using thermal infrared remote sensing, Remote Sens. Environ., 60, 195–216, doi:10.1016/S0034-4257(96)00215-5, 1997.

Anderson, M. C., Norman, J. M., Mecikalski, J. R., Torn, R. D., Kustas, W. P., and Basara, J. B.: A multiscale remote sensing model for disaggregating regional fluxes to micrometeorological scales, J. Hydrometeorol., 5, 343–363, 2004.

Anderson, M. C., Kustas, W. P., Norman, J. M., Hain, C. R., Mecikalski, J. R., Schultz, L., González-Dugo, M. P., Cammalleri, C., d'Urso, G., Pimstein, A., and Gao, F.: Mapping daily evapotranspiration at field to continental scales using geostationary and polar orbiting satellite imagery, Hydrol. Earth Syst. Sci., 15, 223–239, doi:10.5194/hess-15-223-2011, 2011.

Boulet, G., Olioso, A., Ceschia, E., Marloie, O., Coudert, B., Rivalland, V., Chirouze, J., and Chehbouni, G.: An empirical expression to relate aerodynamic and surface temperatures for use within single-source energy balance models, Agr. Forest Meteorol., 161, 148–155, doi:10.1016/j.agrformet.2012.03.008, 2012.

Brutsaert, W.: On a derivable formula for long-wave radiation from clear skies, Water Resour. Res., 11, 742–744, doi:10.1029/WR011i005p00742, 1975.

Brutsaert, W.: Hydrology: an Introduction, Cambridge University Press, 2005.

Colaizzi, P. D., Kustas, W. P., Anderson, M. C., Agam, N., Tolk, J. A., Evett, S. R., Howell, T. A., Gowda, P. H., and O'Shaughnessy, S. A.: Two-source energy balance model estimates of evapotranspiration using component and composite surface temperatures, Adv. Water Resour., 50, 134–151, doi:10.1016/j.advwatres.2012.06.004, 2012.

De Bruin, H. A. R. and Keijman, J. Q.: The Priestley–Taylor Evaporation Model applied to a large, shallow lake in the Netherlands, J. Appl. Meteorol., 18, 898–903, doi:10.1175/1520-0450(1979)018<0898:TPTEMA>2.0.CO;2, 1979.

Detto, M., Montaldo, N., Albertson, J. D., Mancini, M., and Katul, G.: Soil moisture and vegetation controls on evapotranspiration in a heterogeneous Mediterranean ecosystem on Sardinia, Italy, Water Resour. Res., 42, W08419, doi:10.1029/2005WR004693, 2006.

Díaz-Varela, R. A., de la Rosa, R., León, L., and Zarco-Tejada, P. J.: High-resolution airborne UAV imagery to assess olive tree crown parameters using 3D photo reconstruction: application in breeding trials, Remote Sensing, 7, 4213–4232, doi:10.3390/rs70404213, 2015.

Foken, T., Aubinet, M., Finnigan, J. J., Leclerc, M. Y., Mauder, M., and Paw U, K. T.: Results of a panel discussion about the energy balance closure correction for trace gases, B. Am. Meteorol. Soc., 92, ES13–ES18, doi:10.1175/2011BAMS3130.1, 2011.

Gonzalez-Dugo, V., Goldhamer, D., Zarco-Tejada, P. J., and Fereres, E.: Improving the precision of irrigation in a pistachio farm using an unmanned airborne thermal system, Irrigation Sci., 33, 43–52, doi:10.1007/s00271-014-0447-z, 2014.

Guzinski, R., Anderson, M. C., Kustas, W. P., Nieto, H., and Sandholt, I.: Using a thermal-based two source energy balance model with time-differencing to estimate surface energy fluxes with day–night MODIS observations, Hydrol. Earth Syst. Sci., 17, 2809–2825, doi:10.5194/hess-17-2809-2013, 2013.

Guzinski, R., Nieto, H., Jensen, R., and Mendiguren, G.: Remotely sensed land-surface energy fluxes at sub-field scale in heterogeneous agricultural landscape and coniferous plantation, Biogeosciences, 11, 5021–5046, doi:10.5194/bg-11-5021-2014, 2014.

Guzinski, R., Nieto, H., Stisen, S., and Fensholt, R.: Inter-comparison of energy balance and hydrological models for land surface energy flux estimation over a whole river catchment, Hydrol. Earth Syst. Sci., 19, 2017–2036, doi:10.5194/hess-19-2017-2015, 2015.

HESSD

12, 7469–7502, 2015

Harwin, S. and Lucieer, A.: Assessing the accuracy of georeferenced point clouds produced via multi-view stereopsis from unmanned aerial vehicle (UAV) imagery, Remote Sensing, 4, 1573–1599, doi:10.3390/rs4061573, 2012.

Houborg, R., Anderson, M., Gao, F., Schull, M., and Cammalleri, C.: Monitoring water and carbon fluxes at fine spatial scales using HyspIRI-like measurements, in: IEEE International Geoscience and Remote Sensing Symposium (IGARSS), Munich, Germany, 7302–7305, 2012.

Hunt Jr., E. R., Cavigelli, M., Daughtry, C. S., Mcmurtrey III, J. E., and Walthall, C. L.: Evaluation of digital photography from model aircraft for remote sensing of crop biomass and nitrogen status, Precis. Agric., 6, 359–378, 2005.

Kalma, J. D., McVicar, T. R., and McCabe, M. F.: Estimating land surface evaporation: a review of methods using remotely sensed surface temperature data, Surv. Geophys., 29, 421–469, doi:10.1007/s10712-008-9037-z, 2008.

Kustas, W. P. and Norman, J. M.: Use of remote sensing for evapotranspiration monitoring over land surfaces, Hydrolog. Sci. J., 41, 495–516, doi:10.1080/02626669609491522, 1996.

Kustas, W. P. and Norman, J. M.: Evaluation of soil and vegetation heat flux predictions using a simple two-source model with radiometric temperatures for partial canopy cover, Agr. Forest Meteorol., 94, 13–29, doi:10.1016/S0168-1923(99)00005-2, 1999.

Kustas, W. P., Prueger, J. H., and Hipps, L. E.: Impact of using different time-averaged inputs for estimating sensible heat flux of riparian vegetation using radiometric surface temperature, J. Appl. Meteorol., 41, 319–332, 2002.

Liebethal, C. and Foken, T.: Evaluation of six parameterization approaches for the ground heat flux, Theor. Appl. Climatol., 88, 43–56, doi:10.1007/s00704-005-0234-0, 2007.

Lucieer, A., Malenovský, Z., Veness, T., and Wallace, L.: HyperUAS – imaging spectroscopy from a multirotor unmanned aircraft system, J. Field Robot., 31, 571–590, doi:10.1002/rob.21508, 2014.

Mauder, M. and Foken, T.: Impact of post-field data processing on eddy covariance flux estimates and energy balance closure, Meteorol. Z., 15, 597–609, doi:10.1127/0941-2948/2006/0167, 2006.

Moncrieff, J. B., Massheder, J. M., de Bruin, H., Elbers, J. A., Friborg, T., and Heusinkveld, B.: A system to measure surface fluxes of momentum, sensible heat, water vapour and carbon dioxide, J. Hydrol., 188, 589–611, doi:10.1016/S0022-1694(96)03194-0, 1997.

Moncrieff, J., Clement, R., Finnigan, J., and Meyers, T.: Averaging, detrending, and filtering of eddy covariance time series, in: Handbook of Micrometeorology, Springer, available at: http://link.springer.com/chapter/10.1007/1-4020-2265-4_2, last access: 3 June 2015, 7–31, 2005.

Monteith, J. L.: Evaporation and environment, in: Symp. Soc. Exp. Biol, vol. 19, available at: http://www.unc.edu/courses/2007fall/geog/801/001/www/ET/Monteith65.pdf (last access: 17 June 2015), 1965.

Norman, J. M., Kustas, W. P., and Humes, K. S.: Source approach for estimating soil and vegetation energy fluxes in observations of directional radiometric surface temperature, Agr. Forest Meteorol., 77, 263–293, doi:10.1016/0168-1923(95)02265-Y, 1995.

Norman, J. M., Kustas, W. P., Prueger, J. H., and Diak, G. R.: Surface flux estimation using radiometric temperature: a dual-temperature-difference method to minimize measurement errors, Water Resour. Res., 36, 2263–2274, doi:10.1029/2000WR900033, 2000.

Norman, J. M., Anderson, M. C., Kustas, W. P., French, A. N., Mecikalski, J., Torn, R., Diak, G. R., Schmugge, T. J., and Tanner, B. C. W.: Remote sensing of surface energy fluxes at 101-m pixel resolutions, Water Resour. Res., 39, 1221, doi:10.1029/2002WR001775, 2003.

Papale, D., Reichstein, M., Aubinet, M., Canfora, E., Bernhofer, C., Kutsch, W., Longdoz, B., Rambal, S., Valentini, R., Vesala, T., and Yakir, D.: Towards a standardized processing of Net Ecosystem Exchange measured with eddy covariance technique: algorithms and uncertainty estimation, Biogeosciences, 3, 571–583, doi:10.5194/bg-3-571-2006, 2006.

Priestley, C. H. B. and Taylor, R. J.: On the assessment of surface heat flux and evaporation using large-scale parameters, Mon. Weather Rev., 100, 81–92, doi:10.1175/1520-0493(1972)100<0081:OTAOSH>2.3.CO;2, 1972.

Reichstein, M., Falge, E., Baldocchi, D., Papale, D., Aubinet, M., Berbigier, P., Bernhofer, C., Buchmann, N., Gilmanov, T., Granier, A., Grünwald, T., Havránková, K., Ilvesniemi, H., Janous, D., Knohl, A., Laurila, T., Lohila, A., Loustau, D., Matteucci, G., Meyers, T., Miglietta, F., Ourcival, J.-M., Pumpanen, J., Rambal, S., Rotenberg, E., Sanz, M., Tenhunen, J., Seufert, G., Vaccari, F., Vesala, T., Yakir, D., and Valentini, R.: On the separation of net ecosystem exchange into assimilation and ecosystem respiration: review and improved algorithm, Global Change Biol., 11, 1424–1439, doi:10.1111/j.1365-2486.2005.001002.x, 2005.

Ringgaard, R., Herbst, M., Friborg, T., Schelde, K., Thomsen, A. G., and Soegaard, H.: Energy fluxes above three disparate surfaces in a temperate mesoscale coastal catchment, Vadose Zone J., 10, 54, doi:10.2136/vzj2009.0181, 2011.

Santanello, J. A. and Friedl, M. A.: Diurnal covariation in soil heat flux and net radiation, J. Appl. Meteorol., 42, 851–862, 2003.

Shuttleworth, W. J. and Wallace, J. S.: Evaporation from sparse crops – an energy combination theory, Q. J. Roy. Meteorol. Soc., 111, 839–855, 1985.

Stisen, S., Sandholt, I., Nørgaard, A., Fensholt, R., and Jensen, K. H.: Combining the triangle method with thermal inertia to estimate regional evapotranspiration – applied to MSG-SEVIRI data in the Senegal River basin, Remote Sens. Environ., 112, 1242–1255, doi:10.1016/j.rse.2007.08.013, 2008.

Swain, K. C., Thomson, S. J., and Jayasuriya, H. P.: Adoption of an unmanned helicopter for low-altitude remote sensing to estimate yield and total biomass of a rice crop, Trans. ASAE Am. Soc. Agric. Eng., 53, 21–27, 2010.

Turner, D., Lucieer, A., and Watson, C.: An automated technique for generating georectified mosaics from ultra-high resolution unmanned aerial vehicle (UAV) imagery, based on Structure from Motion (SfM) point clouds, Remote Sensing, 4, 1392–1410, doi:10.3390/rs4051392, 2012.

Wallace, L., Lucieer, A., Watson, C., and Turner, D.: Development of a UAV-LiDAR system with application to forest inventory, Remote Sensing, 4, 1519–1543, doi:10.3390/rs4061519, 2012.

Webb, E. K., Pearman, G. I., and Leuning, R.: Correction of flux measurements for density effects due to heat and water vapour transfer, Q. J. Roy. Meteorol. Soc., 106, 85–100, doi:10.1002/qj.49710644707, 1980.

Zarco-Tejada, P. J., González-Dugo, V., Williams, L. E., Suárez, L., Berni, J. A. J., Goldhamer, D., and Fereres, E.: A PRI-based water stress index combining structural and chlorophyll effects: assessment using diurnal narrow-band airborne imagery and the CWSI thermal index, Remote Sens. Environ., 138, 38–50, doi:10.1016/j.rse.2013.07.024, 2013.

Zarco-Tejada, P. J., Diaz-Varela, R., Angileri, V., and Loudjani, P.: Tree height quantification using very high resolution imagery acquired from an unmanned aerial vehicle (UAV) and automatic 3D photo-reconstruction methods, Eur. J. Agron., 55, 89–99, doi:10.1016/j.eja.2014.01.004, 2014.

HESSD

12, 7469–7502, 2015

Estimating evapotranspiration with thermal UAV data

H. Hoffmann et al.

Table 1. UAV retrievals of LST, constituting 12 sets of input data to TSEB-PT and DTD. Early morning flights conducted one hour after sunrise are only used in DTD. (c) means data were collected during cloudy or overcast conditions.

Date		Early flights ($T_{R,0(\theta)}$) Time (UTC)	Daylight flights ($T_{R,i(\theta)}$)				
10 Apr 2014	(c)	07:00			11:30		
22 Apr 2014	(c)	06:00					14:30
15 May 2014		05:30			11:00	12:00	
22 May 2014	(c)	05:00	08:00	09:00	11:30	12:00	
18 Jun 2014	(c)	05:00			11:00	12:00	
2 Jul 2014	(c)	07:30			11:30		
22 Jul 2014		06:30				12:30	

HESSD
12, 7469–7502, 2015
Estimating evapotranspiration with thermal UAV data
H. Hoffmann et al.

Table 2. Measured and modelled net radiation (R_n), sensible heat flux (H) and latent heat flux (LE). Dates marked with (c) represent days with cloudy or overcast conditions.

Date, time (UTC)		Measured ($W\,m^{-2}$) R_n	H	LE	TSEB-PT ($W\,m^{-2}$) R_n	H	LE	DTD ($W\,m^{-2}$) R_n	H	LE
10 Apr 2014 11:30	(c)	243	87	105	155	15	134	155	20	121
22 Apr 2014 14:30	(c)	203	73	81	180	1	181	180	62	118
15 May 2014 11:00		453	124	241	401	42	330	401	75	295
15 May 2014 12:00		619	132	385	600	49	492	600	97	472
22 May 2014 08:00	(c)	270	33	206	284	−20	296	284	95	179
22 May 2014 09:00	(c)	306	−26	290	301	−48	337	301	63	231
22 May 2014 11:30	(c)	406	−16	367	397	−33	418	397	101	287
22 May 2014 12:00	(c)	440	14	365	436	−51	465	436	42	387
18 Jun 2014 11:00	(c)	538	158	326	505	89	397	505	191	309
18 Jun 2014 12:00	(c)	631	200	378	612	54	514	612	156	450
2 Jul 2014 11:30	(c)	217	54	152	121	−9	135	121	52	68
22 Jul 2014 12:30		479	282	161	511	125	335	511	211	293

HESSD
12, 7469–7502, 2015

Estimating evapotranspiration with thermal UAV data

H. Hoffmann et al.

Table 3. Root mean square error (RMSE), mean absolute error (MAE) and correlation coefficient (r) computed for TSEB-PT and DTD results. Values in parenthesis are RMSE and MAE respectively as percentage of measured fluxes.

	RMSE ($W m^{-2}$)			MAE ($W m^{-2}$)			r		
	R_n	H	LE	R_n	H	LE	R_n	H	LE
TSEB-PT	44 (11)	85 (91)	94 (37)	33 (8)	75 (81)	84 (33)	0.98	0.96	0.92
DTD	44 (11)	59 (64)	67 (26)	33 (8)	49 (52)	57 (22)	0.98	0.74	0.85

HESSD
12, 7469–7502, 2015

Estimating evapotranspiration with thermal UAV data

H. Hoffmann et al.

Table 4. Statistical parameters based on data that was collected during only cloudy and overcast weather conditions (9 dates). Root mean square error (RMSE), mean absolute error (MAE) and correlation coefficient (r) computed for TSEB-PT and DTD results. Values in parenthesis are RMSE and MAE respectively as percentage of measured fluxes.

	RMSE ($\mathrm{W\,m^{-2}}$)			MAE ($\mathrm{W\,m^{-2}}$)			r		
	R_n	H	LE	R_n	H	LE	R_n	H	LE
TSEB-PT	40 (11)	63 (99)	69 (27)	32 (8)	64 (100)	71 (28)	0.99	0.84	0.98
DTD	40 (11)	53 (83)	46 (18)	32 (8)	50 (78)	46 (18)	0.99	0.69	0.95

HESSD
12, 7469–7502, 2015

Estimating evapotranspiration with thermal UAV data

H. Hoffmann et al.

Figure 1. HOBE agricultural site in western Denmark (56.037644° N, 9.159383° E). The black square represents location of the eddy flux tower. The green square represents location for zoom inset on the right.

HESSD
12, 7469–7502, 2015

Estimating evapotranspiration with thermal UAV data

H. Hoffmann et al.

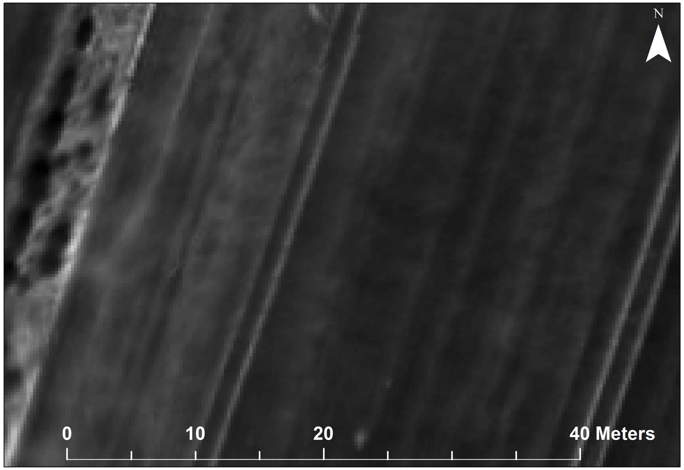

Figure 2. Zoomed inset from thermal mosaic 18 June 2014 12:00 UTC. Black round objects in left hand side of picture represents row of conifers. White stripes in right hand side of picture represents tramlines. Provide a sense of high spatial resolution data.

HESSD
12, 7469–7502, 2015

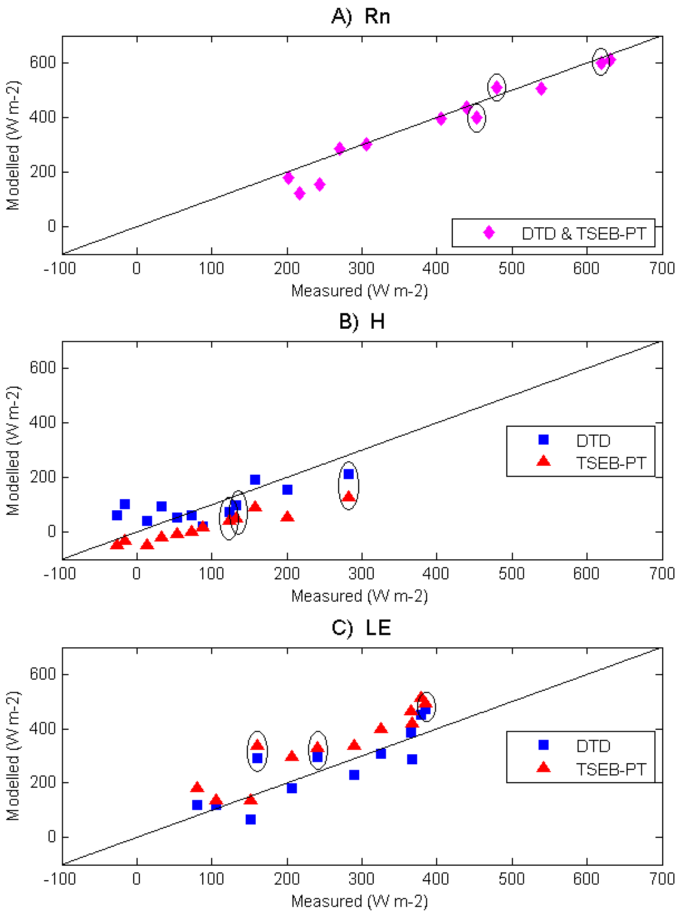

Figure 3. Modelled vs. measured net radiation (R_n), sensible (H) and latent heat fluxes (LE). Data collected in sunny weather conditions are enclosed by black circles.

HESSD
12, 7469–7502, 2015

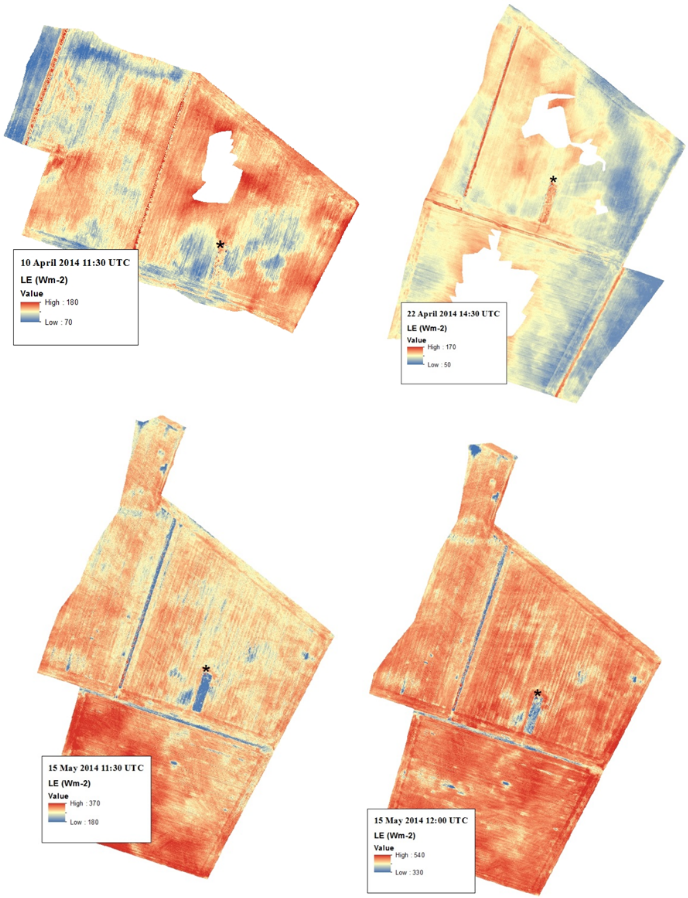

Figure A1a. Evapotranspiration maps from DTD model. Black star represent location of eddy flux tower.

HESSD
12, 7469–7502, 2015

Estimating evapotranspiration with thermal UAV data

H. Hoffmann et al.

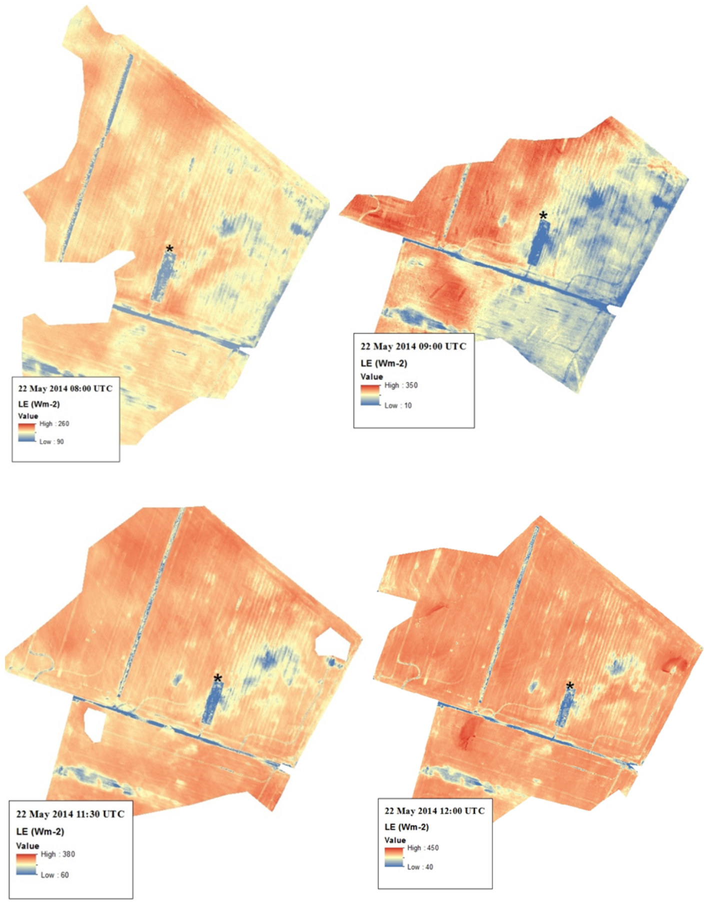

Figure A1b. Evapotranspiration maps from DTD model. Black star represent location of eddy flux tower.

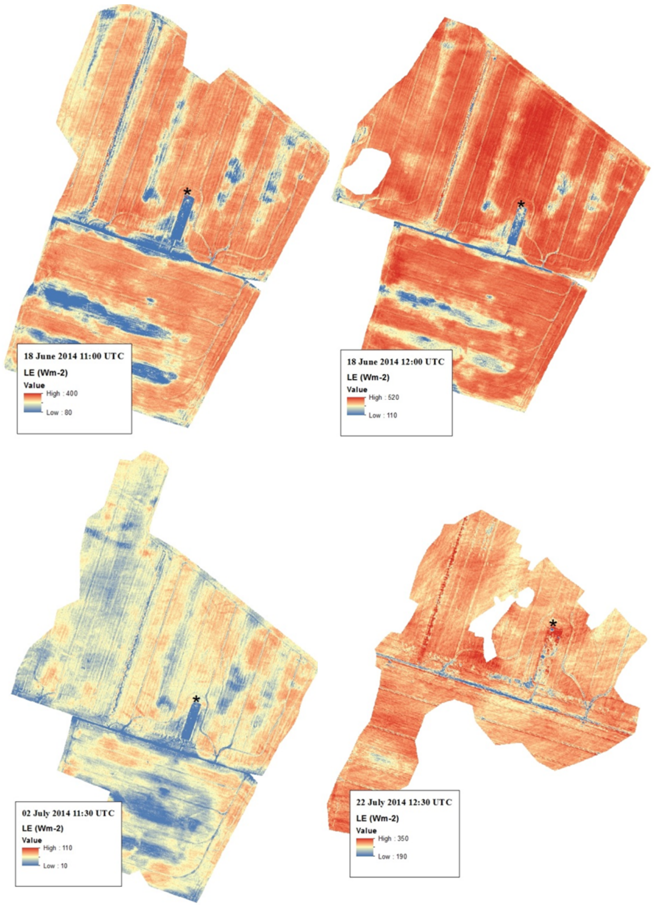

Figure A1c. Evapotranspiration maps from DTD model. Black star represent location of eddy flux tower.

HESSD

12, 7469–7502, 2015